Four-layer nanocomposite structure as an effective optical waveguide switcher for near-IR regime

2016 J. Phys. D: Appl. Phys. 49 435103

(http://iopscience.iop.org/0022-3727/49/43/435103)

IOP Publishing Journal of Physics D: Applied Physics
J. Phys. D: Appl. Phys. **49** (2016) 435103 (10pp) doi:10.1088/0022-3727/49/43/435103

Four-layer nanocomposite structure as an effective optical waveguide switcher for near-IR regime

I S Panyaev[1], N N Dadoenkova[1,2], Yu S Dadoenkova[1,2,3], I A Rozhleys[4], M Krawczyk[5], I L Lyubchanskii[2] and D G Sannikov[1]

[1] Ulyanovsk State University, 432017 Ulyanovsk, Russian Federation
[2] Donetsk Physical and Technical Institute of the National Academy of Sciences of Ukraine, 83114 Donetsk, Ukraine
[3] Novgorod State University, 173003 Veliky Novgorod, Russian Federation
[4] National Research Nuclear University MEPhI, 115409 Moscow, Russian Federation
[5] Faculty of Physics, Adam Mickiewicz University in Poznań, 61-614 Poznań, Poland

E-mail: sannikov-dg@yandex.ru

Received 11 July 2016, revised 1 September 2016
Accepted for publication 13 September 2016
Published 3 October 2016

Abstract

We present a theoretical study of the dispersion and energy properties of the eigenwaves (TE- and TM-modes) in a four-layer structure composed of a magneto-optical yttrium iron garnet guiding layer on a dielectric substrate covered by a planar nanocomposite guiding multilayer. The bigyrotropic properties of yttrium-iron garnet are taken into account for obtaining the dispersion equation and an original algorithm for the guided modes identification is proposed. We demonstrated the polarization switching of TE- and TM-modes dependent on the geometrical parameters of the guiding layers. The dispersion diagrams and field profiles are used to illustrate the change of propagation properties with variation of the multilayer thickness ratio of the nanocomposite's layers. The energy flux distributions across the structure are calculated and the conditions of the optimal guiding regime are obtained. The power switching ratio in the waveguide layers of about 6 dB for the wavelength range of 100 nm is shown to be achieved.

Keywords: waveguide, nanocomposite, long-wave approximation, optical switching

(Some figures may appear in colour only in the online journal)

1. Introduction

Transparent in optical and infrared regimes multilayer structures have been the subjects of intensive theoretical and experimental research because of their wide applications in integrated optics, optoelectronics and photonics during more than forty years [1–11]. The three-layer waveguide usually provides the interconnections in an integrated optical circuits, and it is thus a multilayer structure which forms the actual components of an active or passive devices [12]. The history of investigations of the optical four-layer structures dates back to the late 60s—early 70s when the theory of four-layer isotropic waveguides had been developing [13–15], where a prism was used as a forth (cladding) medium, and an air gap between the prism and the film was considered as a coupling zone, where the fields are evanescent waves. The early experimental measurements of the waveguide modal characteristics have been carried out by Tien *et al* [16] and Sun and Muller [17]. About the same time there was a rapid growth of the heterostructure laser technologies, particularly, the efficient large optical cavity injection lasers were fabricated [18]. A rich variety of the effects and applications of the four-layer structures were studied, for example, the TE/TM polarizers [19], leaky modes lasers [20], optical waveguide lenses and tapered couplers [21], etc. Presence of an extra layer in a conventional three-layer waveguide structure leads to an enhancement of light control options. The metal or semiconductor thin film can be used as the fourth layer, and this means that the

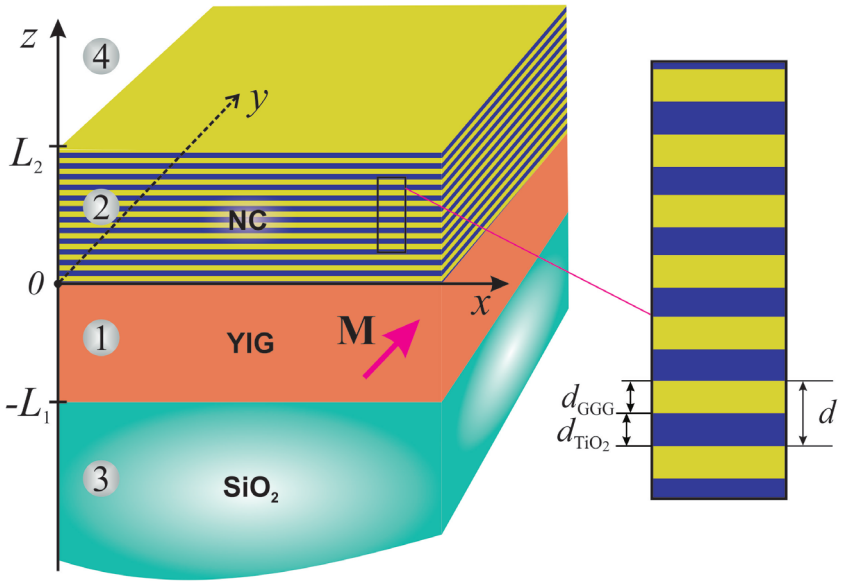

Figure 1. A schematic image of the four-layer structure: layer 1—YIG; layer 2—NC multilayer; layer 3—SiO_2 substrate; layer 4—air.

absorption losses and the mode interaction should be considered [22, 23]. The S-shaped four-layer waveguides were investigated in [24]. The theory had its further mathematical development in obtaining the general (normalized) dispersion relation and founding its application to the control of chromatic dispersion in a thin-film Luneburg lens [12, 25]. The polarization effects as well as the combined effects of the waveguide coupling and losses were determined and illustrated in the devices using the silicon claddings [26]. The semiconductor-based four-layer structure has been studied and proposed as the basic building block for mid-infrared modulators and switches [27, 28].

The investigation of gyromagnetic and gyroelectric properties of the multilayered nanocomposite (NC) structures is of great interest due to their specific properties which make them suitable for wide applications [29]. The optical isolator based on the leaky yttrium iron garnet (YIG) $Y_3Fe_5O_{12}$ waveguide was designed using the transfer matrix formulation [30].

The investigation of the multimode four-layer waveguide structures by modified m-line spectroscopy method was presented in [31]. During the last decade different multilayered waveguiding structures had been studied: the magnetic photonic crystals [32–34], nanocomposite multilayers and photonic crystal waveguides [35], silicon-based hybrid gap surface plasmon polariton waveguides [36], nanophotonic and plasmonic waveguides [37] and multilayer graphene waveguides [38]. Besides, four-layer structures due to the enhanced field confinement in guiding layer [39, 40] can be effectively used in medical applications such as label free biosensors.

In this paper, we investigate theoretically the dispersion and polarization properties of propagating TE- and TM-waves in the hybrid four-layer magneto-optical (MO) nanocomposite waveguide. The multilayered structure is composed of a magneto-optical layer on dielectric substrate covered by multilayered dielectric NC medium. In section 2, using the effective medium approach [41, 42], we obtain the dispersion equation for the multilayered waveguiding structure taking into account bigyrotropic properties of the MO layer and features of the NC topology and propose an algorithm, which unlike the 4×4 matrix method [43] allows to identify the guided modes and to obtain their electric and magnetic fields distributions across the structure. In section 3, we perform the numerical computations for different dispersion dependencies in the conventional telecommunication frequency regimes and present the cross-structure flux distributions. Some possible applications of the structure under consideration are discussed in section 4. In section 5 we summarize the paper results.

2. Theoretical analysis of the complex waveguide structure

2.1. Geometry of the waveguide structure

Let us consider the four-layered waveguide structure consisting of a magneto-optical YIG film of a thickness L_1 on the thick SiO_2 substrate, and covered by a 1D NC multilayer of a thickness L_2, and air playing a role of a cladding. The NC multilayer with the period $d = d_{GGG} + d_{TiO_2}$ is formed by alternating nanolayers of gadolinium-gallium garnet (GGG) $Gd_3Ga_5O_{12}$ and titanium oxide TiO_2 with the corresponding thicknesses d_{GGG} and d_{TiO_2}. We consider the geometry with the layers of the planar structure $(SiO_2/YIG/(GGG/TiO_2)^N/$ air (where N is the number of the NC periods) located in the xy-plane, and the z-axis is perpendicular to the interfaces, as shown in figure 1. The electromagnetic wave propagates along the x-axis, and the magnetization vector $\mathbf{M}$ is transverse to the wave propagation direction and is directed along the y-axis. We assume that in all the layers of the waveguide system (YIG, GGG and TiO_2) the electromagnetic radiation propagates along the x-axis, exponentially decaying in depth of the substrate and air along the z-axis. The considered geometry corresponds to the transverse magneto-optical configuration, and in this case the electromagnetic waves in the YIG layer split into independent TE- and TM-modes [29].

2.2. Material parameters of the constituting layers

It is well known that the YIG is transparent in the near infrared (IR) regime [29, 44] and exhibits bigyrotropic properties, so both dielectric permittivity $\widehat{\varepsilon}_{\mathrm{YIG}}$ and magnetic permeability $\widehat{\mu}_{\mathrm{YIG}}$ tensors contain the nonzero off-diagonal components [45]. For the case of the magnetization **M** along the y-axis, in the linear MO approximation, both tensors have following form [43]:

$$\widehat{\varepsilon}_{\mathrm{YIG}} = \begin{pmatrix} \varepsilon_1 & 0 & \mathrm{i}\varepsilon_a \\ 0 & \varepsilon_1 & 0 \\ -\mathrm{i}\varepsilon_a & 0 & \varepsilon_1 \end{pmatrix}, \quad \widehat{\mu}_{\mathrm{YIG}} = \begin{pmatrix} \mu_1 & 0 & \mathrm{i}\mu_a \\ 0 & \mu_1 & 0 \\ -\mathrm{i}\mu_a & 0 & \mu_1 \end{pmatrix}. \tag{1}$$

From the Maxwell's equations we obtain the following relationships between the electric and magnetic fields components of the electromagnetic wave:

$$\begin{aligned} H_x' + \mathrm{i}\beta H_z &= \mathrm{i}k_0\varepsilon_0 E_y, \\ E_y' &= \mathrm{i}\,k_0(\mu_1 H_x + \mathrm{i}\mu_a H_z), \\ \beta E_y &= k_0(\mu_1 H_z - \mathrm{i}\mu_a H_x), \\ H_y' &= -\mathrm{i}k_0(\varepsilon_1 E_x + \mathrm{i}\varepsilon_a E_z), \\ \beta H_y &= k_0(\mathrm{i}\varepsilon_a E_z - \varepsilon_1 E_z), \\ \mathrm{i}\beta E_z + E_x' &= -\mathrm{i}k_0\mu_0 H_y, \end{aligned} \tag{2}$$

where $k_0 = \omega/c$ is a wave vector of the electromagnetic wave in air (ω is the angular frequency, and c is the speed of light in vacuum), and β is a propagation constant (wave vector component along the x-axis). The permittivity tensors for nonmagnetic dielectrics GGG and TiO_2 are diagonal $\widehat{\varepsilon}_{\mathrm{GGG}} = \varepsilon_{\mathrm{GGG}}\widehat{I}$ and $\widehat{\varepsilon}_{\mathrm{TiO_2}} = \varepsilon_{\mathrm{TiO_2}}\widehat{I}$, where $\widehat{I} = \delta_{ik}$, and δ_{ik} is the Kronecker's delta. In the case of a large number of nanolayers N with the thicknesses d_{GGG} and $d_{\mathrm{TiO_2}}$, satisfying the condition $d_{\mathrm{GGG}},\ d_{\mathrm{TiO_2}} \ll \lambda$ (λ is the wavelength of the electromagnetic wave), one can use the effective medium method (the long-wave approximation), which allows to treat the NC medium as a uniaxial crystal with an effective dielectric permittivity in the form [46]:

$$\widehat{\varepsilon}_{\mathrm{NC}} = \begin{pmatrix} \varepsilon_{xx} & 0 & 0 \\ 0 & \varepsilon_{yy} & 0 \\ 0 & 0 & \varepsilon_{zz} \end{pmatrix} \tag{3}$$

with the tensor components

$$\varepsilon_{xx} = \varepsilon_{yy} = \frac{\Theta\varepsilon_{\mathrm{GGG}} + \varepsilon_{\mathrm{TiO_2}}}{\Theta + 1}, \quad \varepsilon_{zz} = \frac{\varepsilon_{\mathrm{GGG}}\varepsilon_{\mathrm{TiO_2}}(\Theta + 1)}{\Theta\varepsilon_{\mathrm{TiO_2}} + \varepsilon_{\mathrm{GGG}}}, \tag{4}$$

where $\Theta = d_{\mathrm{GGG}}/d_{\mathrm{TiO_2}}$ is the ratio of the GGG and TiO_2 layers thicknesses.

The substrate medium 3 (SiO_2) and the cladding medium 4 (air) have the scalar dielectric permittivities ε_3, ε_4 and magnetic permeabilities $\mu_3 = \mu_4 = 1$. The magnetic permeabilities of GGG, TiO_2 and, therefore, the permeability of NC, are equal to unity ($\mu_2 = 1$).

2.3. Profile functions and dispersion relation

Solving the Maxwell's equations with the given material parameters of all the layers, one can obtain the profile functions of the electric and magnetic fields for TE-and TM-modes. The field of the electromagnetic wave, propagating along the x-axis, is

$$\mathbf{F}(x, z) = \mathbf{F}(z)\mathrm{e}^{\mathrm{i}\beta x}, \tag{5}$$

The tangential components of the vector profile function $\mathbf{F}(z)$ (the electric field component E_y for TE-mode and the magnetic field component H_y for TM-mode) have the form:

$$F_y(z) = A \cdot \begin{cases} \cos h_1 z + \mathrm{C}_1 \sin h_1 z\,, & -L_1 \leqslant z \leqslant 0, \\ \cos h_2 z + \mathrm{C}_2 \sin h_2 z, & 0 \leqslant z \leqslant L_2 \\ [\cos h_1 L_1 - C_1 \sin h_1 L_1]\mathrm{e}^{p(z+L_1)}, & z \leqslant -L_1, \\ [\cos h_2 L_2 + C_2 \sin h_2 L_2]\mathrm{e}^{-q(z-L_2)}, & z \geqslant L_2. \end{cases} \tag{6}$$

Here A is the normalized amplitude which can be calculated by integrating the Poynting vector's longitudinal component [47], the coefficients C_1 and C_2 are determined as:

$$\begin{aligned} C_1 &= \frac{\delta p - h_1 \tan h_1 L_1 - \beta\nu}{\delta p \tan h_1 L_1 + h_1 - \beta\nu \tan h_1 L_1}, \\ C_2 &= \frac{h_2 \tan h_2 L_2 - \sigma q}{h_2 + \sigma q \tan h_2 L_2}, \end{aligned} \tag{7}$$

and the transverse components of the wave vector in each layer are defined as:

$$\begin{cases} h_1^2 = k_0^2\varepsilon_1\mu_\perp - \beta^2 \quad \text{(TE-modes)}, \\ h_1^2 = k_0^2\mu_1\varepsilon_\perp - \beta^2 \ \text{(TM-modes)}, \end{cases}$$
$$\begin{cases} h_2^2 = k_0^2\varepsilon_{yy}\mu_2 - \beta^2 \qquad \text{(TE-modes)}, \\ h_2^2 = k_0^2\varepsilon_{xx}\mu_2 - \dfrac{\varepsilon_{xx}}{\varepsilon_{zz}}\beta^2 \text{(TM-modes)}, \end{cases} \tag{8}$$
$$\begin{cases} p^2 = \beta^2 - k_0^2\varepsilon_3, \\ q^2 = \beta^2 - k_0^2\varepsilon_3, \end{cases}$$

where $\sigma = \mu_2/\mu_4$, $\tau = \mu_\perp/\mu_2$, $\delta = \mu_\perp/\mu_3$, $\nu = \mu_a/\mu_1$ for TE-mode, and $\sigma = \varepsilon_{xx}/\varepsilon_4$, $\tau = \varepsilon_\perp/\varepsilon_{xx}$, $\delta = \varepsilon_\perp/\varepsilon_3$, $\nu = \varepsilon_a/\varepsilon_1$ for TM-mode, with $\mu_\perp = \mu_1 - \mu_a^2/\mu_1$ and $\varepsilon_\perp = \varepsilon_1 - \varepsilon_a^2/\varepsilon_1$ being the transverse magnetic permeability and dielectric permittivity, respectively. The dispersion equation which connects the propagation constant β of the corresponding waveguide mode with the angular frequency and waveguide structure parameters can be obtained from the continuity conditions for the tangential field components at the boundaries of the media and can be written as

$$\begin{aligned} &[\delta\tau\, p h_2^2 + \sigma q h_1^2 + \beta\nu(\beta\nu\sigma q - \delta\sigma p q - \tau h_2^2)]\tan h_1 L_1 \cdot \tan h_2 L_2 \\ &+ h_2[h_1^2 - \delta\sigma\tau p q + \beta\nu(\beta\nu + \tau\sigma q - \delta p)]\tan h_1 L_1 \\ &+ h_1(\tau h_2^2 - \delta\sigma p q)\tan h_2 L_2 - h_1 h_2(\delta p + \sigma\tau q) = 0\,. \end{aligned} \tag{9}$$

Another form of the dispersion equation for a non-gyrotropic media is obtained in [16, 17] and the similar one is given in [48, 49]. In the absence of the NC layer ($L_2 = 0$), the equation (9) transforms into a well-known dispersion equation for a three-layer waveguide structure (see, e.g. [1, 50]).

Table 1. Sellmeier coefficients in equation (13).

Material	A_1	A_2	A_3	B_1 (μm)	B_2 (μm)	B_3 (μm)
YIG [51]	3.739	0.79	—	0.28	10	—
GGG [52]	1.7727	0.9767	4.9668	0.1567	0.01375	22.715
SiO_2 [53]	0.696 1663	0.407 9426	0.897 4794	0.068 4043	0.116 2414	9.896 161

2.4. Guiding mode identification

In order to determine the number of nodes of the electric and magnetic fields for TE- and TM-modes, we rewrite the profile functions (6) for the layers 1 and 2 in the following form:

$$\begin{cases} F_y(-L_1 \leqslant z \leqslant 0) = A \cdot \mathrm{sign}(C_1)\sqrt{1+C_1^2}\ \sin(h_1 z + \varphi_1), \\ F_y(0 \leqslant z \leqslant L_2) = A \cdot \mathrm{sign}(C_2)\sqrt{1+C_2^2}\ \sin(h_2 z + \varphi_2). \end{cases} \tag{10}$$

Here $\varphi_1 = \arctan(1/C_1)$ and $\varphi_2 = \arctan(1/C_2)$ are the initial phases. The number of nodes can be defined as follows. In the chosen layer, for example, the layer 1 (YIG), if the initial phase φ_1 satisfies the condition $0 \leqslant \varphi_1 \leqslant |h_1 L_1| - \pi \cdot \{|h_1 L_1|/\pi\}_{\mathrm{int}}$ (the subscript 'int' denotes the integer part), then the number of nodes M_1 in the layer is equal to $M_1 = \{|h_1 L_1|/\pi\}_{\mathrm{int}} + 1$. In all other cases the number of nodes is less by 1: $M_1 = \{|h_1 L_1|/\pi\}_{\mathrm{int}}$. The number of nodes in the layer 2 (NC), M_2 is defined in the similar way:

$$\begin{cases} M_2 = \{h_2 L_2/\pi\}_{\mathrm{int}} + 1, \ \text{if } \pi \cdot \{h_2 L_2/\pi\}_{\mathrm{int}} - h_2 L_2 \leqslant \varphi_2 \leqslant 0, \\ M_2 = \{h_2 L_2/\pi\}_{\mathrm{int}}, \ \text{in all other cases.} \end{cases} \tag{11}$$

Then, the order of the mode is determined as:

$$M = M_1 + M_2. \tag{12}$$

3. Numerical results and discussion

For the numerical analysis of the results obtained above, we take into account the dispersion of refractive indexes (the Sellmeier's equations) of YIG, SiO_2, GGG:

$$n^2 = 1 + \frac{A_1\lambda^2}{\lambda^2 - B_1^2} + \frac{A_2\lambda^2}{\lambda^2 - B_2^2} + \frac{A_3\lambda^2}{\lambda^2 - B_3^2}. \tag{13}$$

The coefficients A_i and B_i (where $i = 1,2,3$) are given in table 1. As for TiO_2, its dispersion is given by formula $n^2_{TiO_2} = 5.913 + \frac{0.2441}{\lambda^2 - 0.0803}$ [54].

For GGG, TiO_2 and SiO_2 layers we obtain the following wavelength-dependent dielectric permittivities: $\varepsilon_{GGG}(\lambda) = n^2_{GGG}(\lambda)$, $\varepsilon_{TiO_2}(\lambda) = n^2_{TiO_2}(\lambda)$, $\varepsilon_3(\lambda) = n^2_{SiO_2}(\lambda)$. For the YIG layer, the diagonal components of the dielectric permittivity tensor $\hat{\varepsilon}_{YIG}$ in (1) are assumed to be $\varepsilon_1 = n^2_{YIG}(\lambda)$. According to [55], the off-diagonal material tensor elements for YIG are $\varepsilon_a = -2.47 \cdot 10^{-4}$ and $\mu_a = 8.76 \cdot 10^{-5}$. The magnetic permeability components of YIG can be taken as $\mu_1 = 1$ for the considered frequency regime [45].

The refractive indices of the NC multilayer and YIG film can be obtained from the wave localization conditions $h_1 = 0$ and $h_2 = 0$ (see equation (8)). Thus, for the NC multilayer $n_2^{TE} = \sqrt{\varepsilon_{yy}\mu_2}$, $n_2^{TM} = \sqrt{\varepsilon_{zz}\mu_2}$ and for the YIG film $n_1^{TM} = \sqrt{\varepsilon_{\perp}\mu_1}$ and $n_1^{TE} = \sqrt{\varepsilon_1\mu_{\perp}}$. It should be noted, that in the NC multilayer the refractive indices for TE- and TM-modes differ considerably, and an inequality $n_2^{TE} > n_2^{TM}$ is satisfied throughout the entire wavelength range for all values of Θ, as it follows from equations (4). The difference between n_2^{TE} and n_2^{TM} varies with Θ and depends on the dielectric permittivities of the NC constituents. Also, the difference shows the anisotropy of optical properties of TE- and TM-modes which is only due to the nanostructuring of the waveguide layer 2. In the YIG film the refractive indices n_1^{TE} and n_1^{TM} are almost equal due to the small off-diagonal components of dielectric permittivity and magnetic permeability tensors in the considered wavelength range, so below we assume that $n_1^{TE} \approx n_1^{TM} \equiv n_1$.

In figure 2 we present the dispersion of the refractive indices calculated within $\lambda = (1 \div 6)$ μm for different values of the ratio between the thicknesses of GGG and TiO_2 layers constituting the NC multilayer: (a) $\Theta = 0.5$, (b) $\Theta = 0.62$, (c) $\Theta = 1$, and (d) $\Theta = 1.75$. The solid, dashed and dot-dashed lines denote $n_2^{TE}(\lambda)$, $n_2^{TM}(\lambda)$ and $n_1(\lambda)$, respectively.

As one can see from figure 2, for the fixed wavelength, one of the following conditions can be satisfied:

$$n_1 < n_2^{TM} < n_2^{TE}, \tag{14a}$$

$$n_2^{TM} < n_1 < n_2^{TE}, \tag{14b}$$

$$n_2^{TM} < n_2^{TE} < n_1. \tag{14c}$$

The dispersion curves of the waveguide modes propagating in both layers (YIG and NC) are located between the curves $n_3(\lambda) = \sqrt{(\epsilon_3\mu_3)}$ and min (n_1, n_2^{TE}) or min(n_1, n_2^{TM}). Below we follow the terminology introduced by Adams [50] and call the waveguide modes guided by both YIG and NC layers as the modes of A-regime, and the modes guided by only one of these layers as the modes of B-regime.

As can be seen from figures 2(a)–(d), the increase of Θ leads to decrease of both n_2^{TE} and n_2^{TM}. Varying Θ one can satisfy one or another condition of equations (14*a*)–(14*c*). Thus, for $\Theta = 0.5$ (see figures 2(a)), the condition (14*a*) is valid for all wavelength range under consideration: 1.0 μm $< \lambda <$ 6.0 μm. The increase of Θ to 0.62 (figures 2(b)) leads to the intersection of the dispersion curves of n_2^{TM} and n_1 at $\lambda = 1.2$ μm, so that for 1 μm $< \lambda <$ 1.2 μm the condition (14*b*) takes place, while for 1.2 μm $< \lambda <$ 6.0 μm the condition (14*a*) is still valid). For $\Theta = 1$ (see figures 2(c)), the condition (14*b*) is satisfied for 1.2 μm $< \lambda <$ 6.0 μm, while for $\lambda <$ 1.2 μm

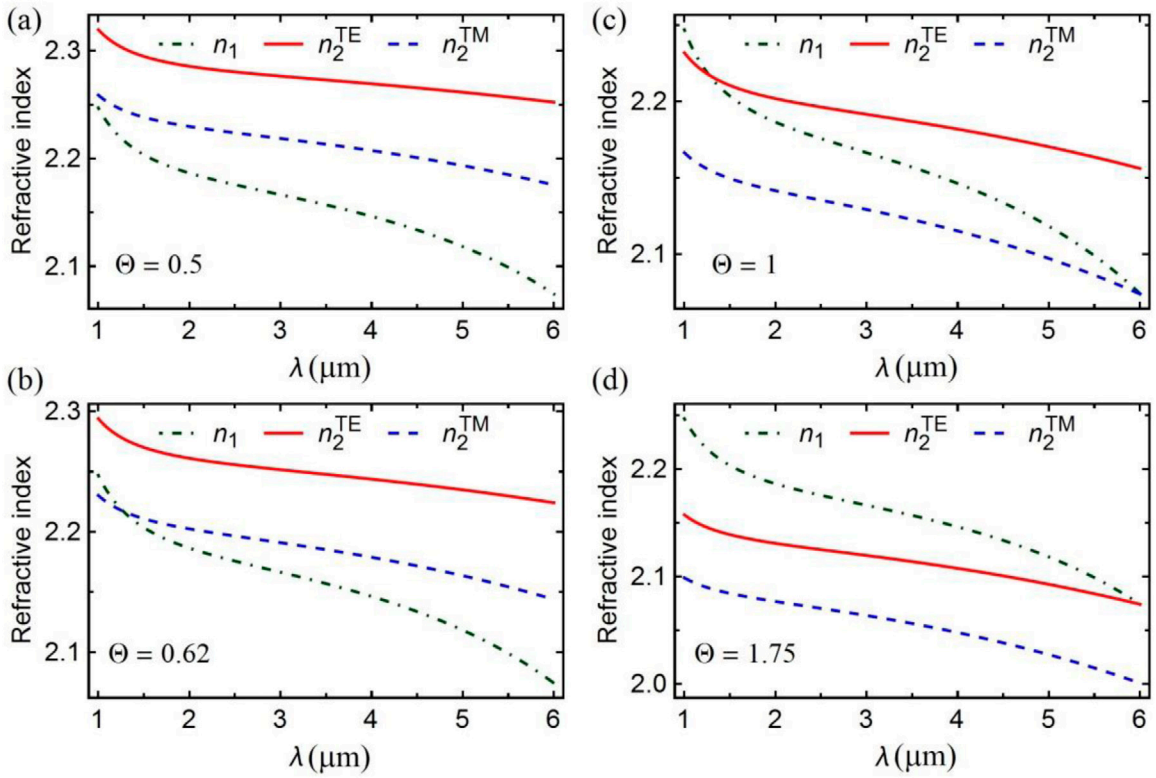

Figure 2. Refractive indices dispersion for different values of Θ: 0.5 (a), 0.62 (b), 1 (c), and 1.75 (d). The solid, dashed and dot-dashed lines correspond to $n_2^{TE}(\lambda)$, $n_2^{TM}(\lambda)$ and $n_1(\lambda)$, respectively.

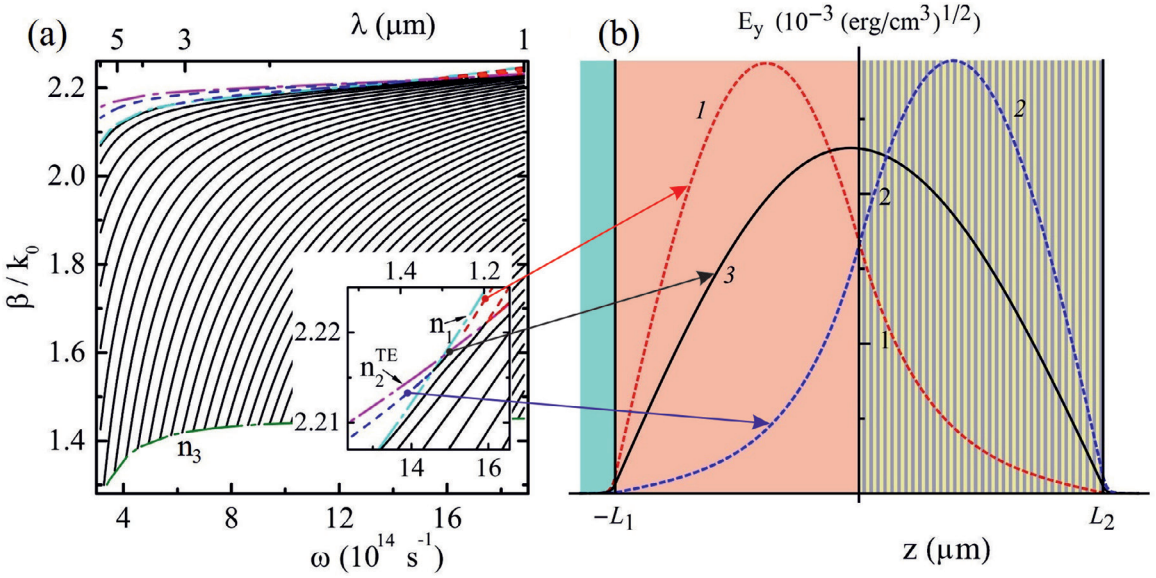

Figure 3. (a) The effective mode indices for TE-modes β/k_0 versus frequency ω; (b) profile functions within the waveguide layers for the fundamental mode TE_0 for λ =1.2 μm, 1.27 μm and 1.4 μm (the lines marked with numbers 1, 2 and 3, respectively and connected with the corresponding points of the dispersion curves by arrows). The calculations are carried out for $L_1 = L_2 = 7$ μm and $\Theta = 1$.

the condition (14*c*) takes place. The further increase of Θ to 1.75 ensures the validity of the condition (14*c*) for all considered wavelength range $\lambda = (1 \div 6)$ μm.

In figure 3(a) we present the spectra for TE-modes in the wavelength range $\lambda = (1 \div 6)$ μm. The calculations are performed for $L_1 = L_2 = 7$ μm and $\Theta = 1$. The corresponding profile function, i.e. the field distributions within the guiding layers for the fundamental TE_0 mode for $\lambda = 1.2$ μm, 1.27 μm and 1.4 μm, are shown in figure 3(b). It should be noted that each dispersion curve is characterized by the corresponding mode number M (see the equation (12)), which does not change with the frequency. In figure 3(a), at the fixed frequency ω one can enumerate the mode from top to bottom: the fundamental mode with $M = 0$ is the highest one (the dashed

blue line) and has the largest effective index, the first one has a smaller index, and so on. The dashed lines correspond to the B-regime modes. The modes located in the area $n \in (n_1, n_2)$ (where $n_1 < n_2^{TE}$) propagate in the layer 2 (NC multilayer), while the modes from the region $n \in (n_2, n_1)$ (where $n_2^{TE} < n_1$) propagate in the layer 1 (YIG). The corresponding field profiles are depicted in figure 3(b).

In order to estimate the feasible value of the normalized coefficient A in the equation (10), let us take the intensity of the input laser beam to be $I = P/\pi r^2 \approx 10\,\mathrm{W\,cm^{-2}}$, where $r = 0.01$ cm is the beam radius and output laser power $P \approx 3$ mW. Considering the geometry of the structure, we assume the input laser beam transforms within the structure into a spot of the elongated ellipse shape with the area $\pi ab \approx \pi r^2$, where a and b are the major (along the y-axis) and minor (along the z-axis) axes of the ellipse, respectively. Thus, taking $a \approx 0.1$ cm and $b \approx 10\,\mu$m (i.e. guiding film width and thickness), we obtain the value of the power per unit length along the y-axis of the order of 1 W m^{-1}, which is in agreement with the conventional values (see, e.g. monograph of *A.Yariv* [3]). Thus, for TE-mode the normalization coefficient $A^2 = 8\pi/(c\int_{-\infty}^{\infty} E_y H_z \mathrm{d}z)$ is of the order of 10^{-6} (erg cm^{-3}).

However, as mentioned before, the asymptotes n_1 and n_2 can intersect at different values of λ, depending on Θ. From figure 3(b) and the inset in figure 3(a), one can see that the TE$_0$-mode transforms from the mode, guided by the layer 2 (the dashed blue curve 2 in figure 3(b)), to the mode, guided by the layer 1 (the dashed red curve 1 in figure 3(b)), passing through the area, where it propagates in the regime A, i.e. to the mode, guided by both layers (solid curve 3 in figure 3(b)). The similar situation can be observed for the TM$_0$-mode, but for another value of Θ, as the dispersion curves of n_2^{TE} and n_2^{TM} can intersect the asymptote n_1 at the same wavelength (frequency) in the case of the different values of Θ (see figures 2(b) and (c)).

In figure 4 we demonstrate the dispersion spectra β/k_0 versus L_1/λ_0 for TE- (solid red lines) and TM-modes (dashed blue lines) for the cases: (a) $\Theta = 0.3$, (b) Θ =0.8, (c) $\Theta = 2.0$ calculated for $\lambda_0 = 1.55$ μm, $L_2 = 1.5$ μm. The horizontal dash-dotted lines denote n_1, n_2 and n_3. Depending on the value of Θ the relation between n_1, n_2^{TE} and n_2^{TM} changes (see equations (14*a*)–(14*c*)), as depicted in the insets. In the shaded areas in figures 4 and 5, TE- and TM-modes switch from the A- to B-regime, while the modes of both polarizations in the other areas in the figures refer to A-regime only. It means that the shaded areas correspond to the regions where the guiding modes can be localized both within YIG and NC layers (i.e. A-regime) or within only one of the layers (i.e. B-regime). In figure 4(a) one can see, that TE- and TM-modes visibly differ almost in all considered range of L_1/λ_0. With the increase of the YIG layer thickness the dispersion curves concentration of the A-regime modes takes place (particularly, all modes between the n_3 and n_1 asymptotes), while the B-regime modes with the effective indices located between the n_1 and n_2^{TE} (namely, the TE$_0$-, TE$_1$- and TM$_0$-modes) are not subjected to such a concentration, as one can see in the inset in figure 4(a). Here, in the inset,

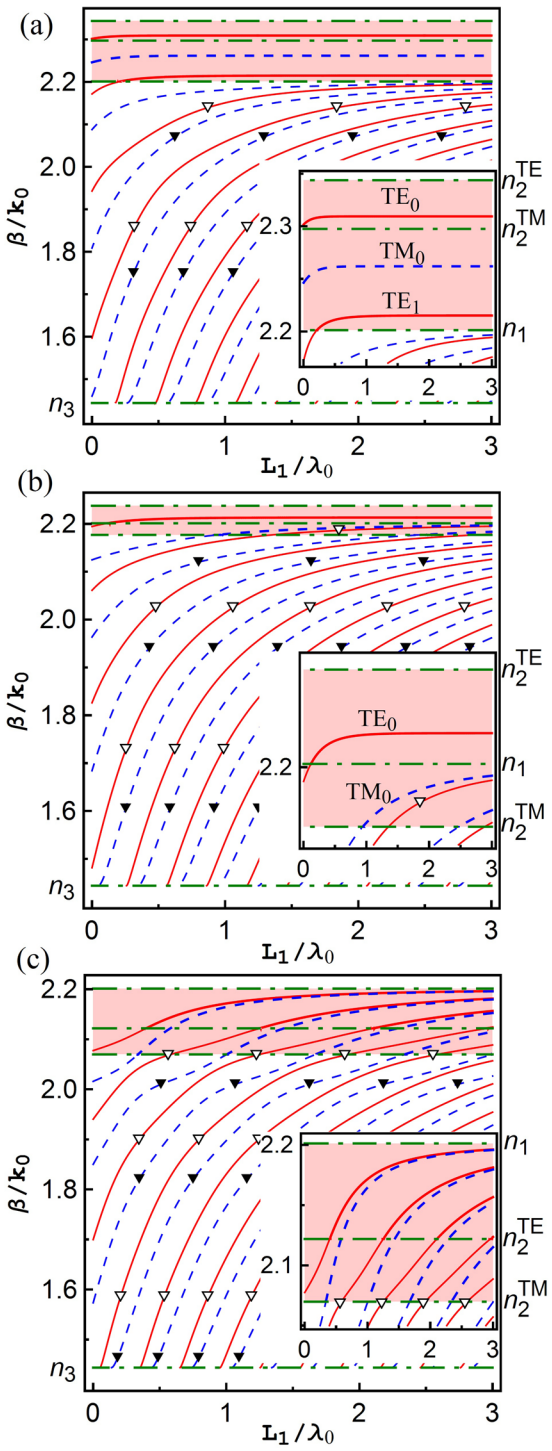

Figure 4. Dispersion spectra β/k_0 versus L_1/λ_0 for TE- (solid red lines) and TM-modes (dashed blue lines) for the cases: (a) $\Theta = 0.3$, (b) $\Theta = 0.8$, (c) $\Theta = 2.0$ calculated for $\lambda_0 = 1.55$ μm, $L_2 = 1.5$ μm. The dash-dotted lines denote n_1, n_2 and n_3.

with the increase of L_1/λ_0 the dispersion curve for TE$_1$ mode intersects the asymptote n_1 and the mode switches from A- to B-regime (i.e. the condition (14*a*) is satisfied and TE$_1$ mode is now localized in the NC layer).

An important peculiarity of the considered structure is that for $\Theta = 0.8$ and in the vicinity of this value (see figure 4(b)) the condition $n_2^{TM} < n_1 < n_2^{TE}$ is satisfied, which, in turn, leads to an

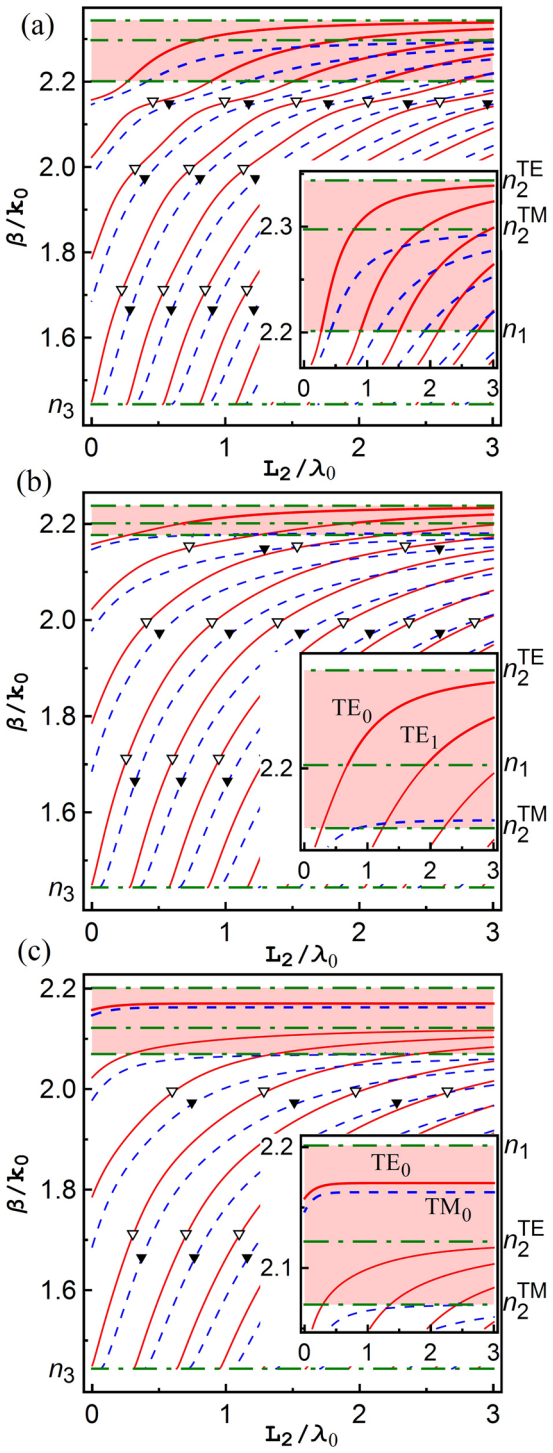

Figure 5. The same as in figure 4, except for β/k_0 versus L_2/λ_0, $L_1 = 1.5\ \mu$m. The non-shaded areas in figures 4 and 5 refer to the A-regime for the modes of both polarizations.

'inversed' localization of the waves guided in the B-regime: the TE_0-mode propagates in the NC-layer, whereas the TM_0- and TM_1-modes propagate in the YIG-layer. For $\Theta = 2$ (the inset in figure 4(c)) the TE- and TM-modes exhibit a tendency to degeneration (i.e. their dispersion curves almost merge) that is much stronger in the B-regime than in the A-regime. Unlike the case depicted in figure 4(a), where only the high-order TE- and TM-modes transfer into the B-regime, here all the modes (both TE- and TM-polarized) convert from the A- to B-regime. Specifically, in the area $\beta/k_0 \in (n_2^{TE}, n_1)$ all modes are the guiding modes of the YIG-layer.

The triangles in figures 4 and 5 (white ones for TE- and black ones for TM-modes) indicate the points where the profile functions (i.e. $E_y(z)$ for TE- and $H_y(z)$ for TM-modes) turn to zero at the interface of the guiding layers ($F_y(0) = 0$). In other words, at these points the electric or magnetic field node passes through the boundary between the guiding layers. The condition of zero field amplitude at the boundary follows from the requirements $C_1, C_2 \to \infty$:

$$h_1 L_1 + \arctan[h_1/(\delta p - \beta\nu)] = \pi l,$$
$$h_2 L_2 + \arctan[h_2/\sigma q] = \pi l, \qquad (15)$$

where $l = 1, 2, 3...$ is an index of the passing node. The intersections of the solutions of equations (15) with the dispersion curves of the guided modes give the zero field points (the triangles in figures 4 and 5).

It should be mentioned, that the number of nodes in the guiding layer grows with the increase of its thickness [50].

In figure 5 we show the dependence of β/k_0 on the normalized NC-layer thickness L_2/λ_0. The solid red lines and dashed blue lines correspond to TE- and TM-modes, respectively, the dash-dotted lines denote n_1, n_2 and n_3 for the cases: (a) $\Theta = 0.3$, (b) $\Theta = 0.8$, (c) $\Theta = 2.0$. The calculations are carried out for $\lambda_0 = 1.55\ \mu$m and $L_1 = 1.5\ \mu$m.

Comparing figures 4 and 5, one can observe a significant difference in the modes behavior depending on the type of the layer which thickness is changing. Specifically, with the increase of L_2/λ_0 all modes (both TE and TM modes) become the B-regime modes for $\Theta = 0.3$ (see figure 5(a)). All TE-modes and only one TM_0-mode transform to the B-regime for $\Theta = 0.8$ (figure 5(b)), and only the fundamental TE_0- and TM_0-modes are the modes of the B-regime for $\Theta = 2$ (figure 5(c)). In the latter case TE_0- and TM_0-modes remain the B-regime modes independently on L_2/λ_0. Moreover, the increase of L_2/λ_0 also affects the mode degeneration character: one can observe not the concentration, but the intersections of the dispersion curves for different order modes.

The longitudinal Poynting vector components which characterize the power fluxes across the waveguide structure are given by

$$S_x^{TE} = \frac{c}{8\pi}\mathrm{Re}(E_y H_z), \quad S_x^{TM} = -\frac{c}{8\pi}\mathrm{Re}(H_y E_z) \qquad (16)$$

for TE- and TM-modes, respectively.

Figure 6 illustrates the power flux density redistribution across the structure with the change of the wavelength. For TE_0-mode, the flux density peak shifts from the center of YIG layer to the center of NC-multilayer with wavelength increasing from 1.0 μm to 1.4 μm (see figure 6(a)), i.e. the switching between the guiding layers takes place. The envelope curve shows the abrupt lowing of the flux density maximum when the peak reaches the YIG-NC interface. For TM_0-mode, the analogous switching takes place at the wavelength interval between 1.4 μm and 1.7 μm and it is more smooth then for TE_0-mode (see figure 6(b)).

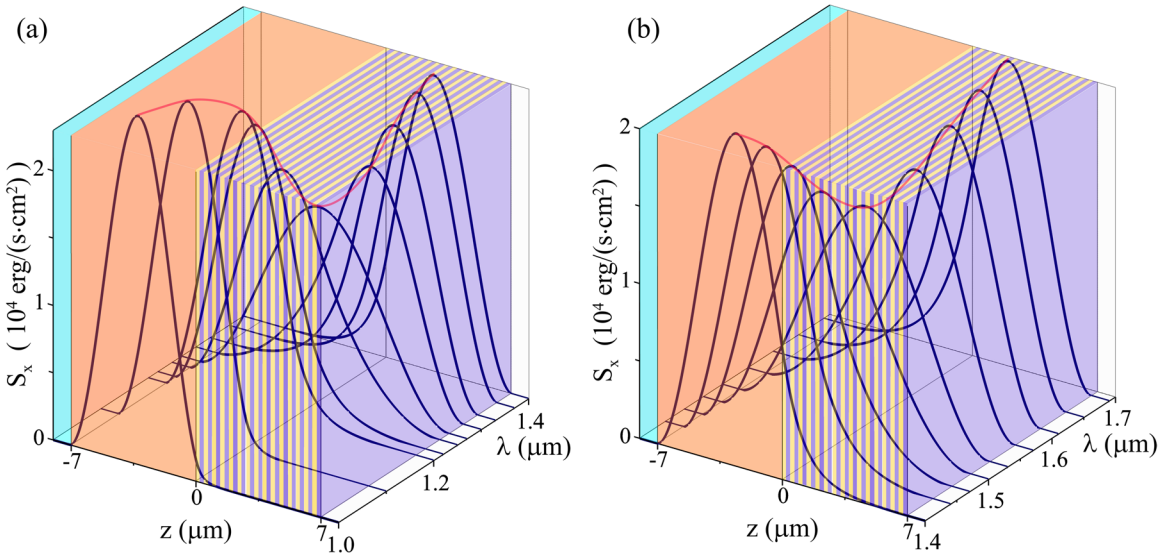

Figure 6. Distribution of the longitudinal component of Poynting's vector as a function of wavelength for the fundamental TE_0- (a) and TM_0-modes (b) for $L_1 = L_2 = 7\ \mu$m, $\Theta = 1.01$ (a) and $\Theta = 0.66$ (b).

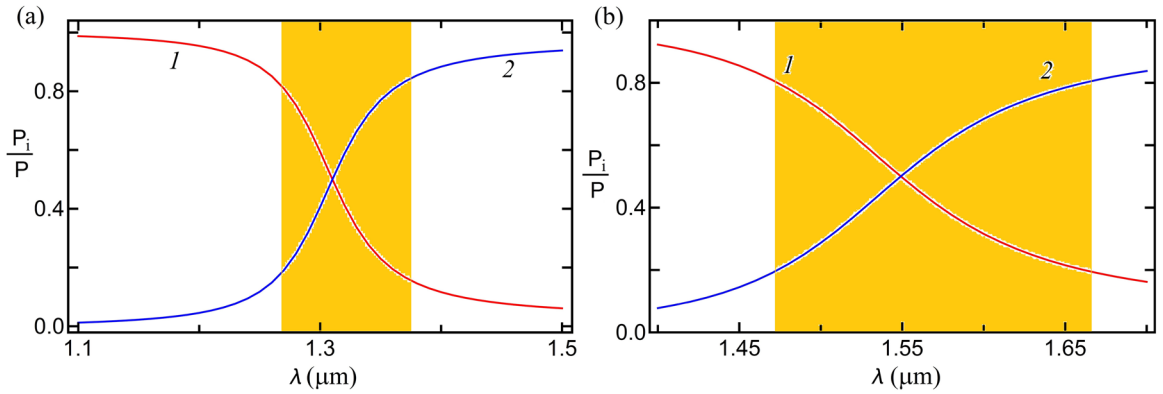

Figure 7. The power flux portions P_i/P as a function of wavelength for the fundamental TE_0- (a) and TM_0-modes (b) (the indices $i = 1, 2$ denote the YIG- and NC-layers); $L_1 = L_2 = 7\ \mu$m, $\Theta = 1.01$ (a) and $\Theta = 0.66$ (b); the shaded areas denote the switching range.

4. Power flux analysis

The spectra of TE-modes (see the inset in figure 3(a)) allow the three different mode propagation regimes within the wavelength regime $\lambda \approx (1.1 \div 1.6)\ \mu$m. So, one can control the electromagnetic wave amplitude in the different guiding layers by adjusting its wavelength, as figure 7 illustrates. The peak of the power flux $P = \int_{-\infty}^{\infty} S_x \mathrm{d}z$ moves from the YIG-layer to the NC-multilayer with the increase of the wavelength: the part of the energy carried by the YIG-layer decreases, while that of the NC-layer grows. The partial power fluxes are defined as $P_1 = \int_{-L_1}^{0} S_x \mathrm{d}z$ in the YIG-layer and $P_2 = \int_{0}^{L_2} S_x \mathrm{d}z$ in the NC-multilayer. The values of the nanolayers thicknesses ratio Θ are chosen to satisfy the condition of the equal power flux distribution between the waveguiding layers at the wavelength $\lambda = 1.31\ \ \mu$m for the TE-polarization (figure 7(a)) and at $\lambda = 1.55\ \ \mu$m for the TM-polarization (figure 7(b)).

The logarithmic power switching ratio $\eta = 10 \log_{10}(P_1/P_2)$ of the order of 6 dB and higher in the wavelength range of about 100 nm can be achieved for TE_0 mode (figure 7(a)). For TM_0 mode (figure 7(b)) a similar switching appears in a twice wider wavelength range (~200 nm). Therefore, a wavelength-tunable optical switch can be constructed on the base of the given structure with the possibility of changing the logical state of the waveguide optical cell. Note that for coupling of the waveguide with the laser light into some coupling schemes can be used: end-fire coupling by a lens or by an optical fiber, prism- or grating-assisted coupling (see, e.g. [56]). Moreover, the structure can be used as a two-channel polarization splitter at the fixed λ, where the TE_0-mode propagates in one layer and the TM_0-mode propagates in another one.

5. Conclusion

In conclusion, we analyzed peculiarities of the waveguide propagation in the four-layer nanocomposite-based MO waveguide structure and demonstrated unique characteristics of its eigenwaves, particularly, polarization switching of TE- and TM-modes depending on the geometrical parameters of the guiding layers. The dispersion relation is obtained taking into account bigyrotropy of the magnetic layer and properties of

the nanocomposite layer topology, and an original algorithm of the guided modes identification is proposed.

Our analysis gives better understanding of the evolution of the modes in a four-layer nanocomposite-based bigyrotropic waveguide structures and demonstrates the advantage of the nanocomposite layer in comparison to the homogeneous one in the case of optical switching, opening up a new way forward for the effective using of the similar NC structures. The waveguide propagation regime switching, due to the polarization filtration occurs depending on the geometry parameters (passive guiding light control) of the structure and wavelength (the so-called λ-tuning).

To summarize, along with low optical losses of the constituting materials at the conventional telecommunications wavelengths the discussed above features of the structure under consideration can find its applications in designing asymmetric and bidirectional optoelectronic and nanophotonic devices such as optical switchers, modulators, isolators which are using for the signal modulation/switching [57, 58]. It is also important to note that, considering a gyrotropy of YIG, one can use the structure for an accumulation of the gyrotropy effect in a microresonator photonic cavity.

Acknowledgments

This research has received funding from the European Union's Horizon 2020 research and innovation programme under the Marie Skłodowska-Curie grant agreement No. 644348 (NND, YuSD, MK and ILL), MPNS COST Action MP1403 'Nanoscale Quantum Optics' (NND, YuSD and ILL), is supported by the grant from Ministry of Education and Science of Russian Federation: Project No. 14.Z50.31.0015 and No. 3.2202.2014/K (NND, YuSD, ISP and DGS) and also is supported by Ukrainian State Fund for Fundamental Research: No. Ф71/73-2016 'Multifunctional Photonic Structures' (ILL).

References

[1] Barnoski M K 1974 *Introduction to Integrated Optics* (New York: Plenum)
[2] Tamir T 1975 *Integrated Optics* (Berlin: Springer)
[3] Yariv A and Yeh P 1984 *Optical Waves in Crystals* (New York: Wiley)
[4] Vetrov S Y, Bikbaev R G and Timofeev I V 2013 Optical Tamm states at the interface between a photonic crystal and a nanocomposite with resonance dispersion *J. Exp. Theor. Phys.* **117** 988
[5] Vetrov S Y, Bikbaev R G and Timofeev I V 2016 Optical Tamm states at the interface between a photonic crystal and a nanocomposite containing core–shell particles *J. Opt.* **10** 065106
[6] Hunsperger R G 2009 *Integrated Optics: Theory and Technology* vol 2 (New York: Springer)
[7] Okamoto K 2006 *Fundamentals of Optical Waveguides* vol 53 (Amsterdam: Elsevier)
[8] Wang X, Yin C and Cao Z 2016 *Progress in Planar Optical Waveguides* (Shanghai: Springer)
[9] Boardman A D 1982 *Electromagnetic Surface Modes* (New York: Wiley)
[10] Lee D L 1986 *Electromagnetic Principles of Integrated Optics* (Somerset, NJ: Wiley)
[11] Syms R and Cozens J 1992 *Optical Guided Waves and Devices* (Maidenhead: McGraw-Hill)
[12] Hewak D W and Lit J W Y 1987 Generalized dispersion properties of a four-layer thin-film waveguide *Appl. Opt.* **26** 833–41
[13] Tien P K, Ulrich R and Martin R J 1969 Modes of propagating light waves in thin deposited semiconductor films *Appl. Phys. Lett.* **14** 291–4
[14] Tien P K and Ulrich R 1970 Theory of prism-film coupler and thin-film light guides *J. Opt. Soc. Am.* **60** 1325–37
[15] Tien P K, Smolinsky G and Martin R J 1972 Thin organosilicon films for integrated optics *Appl. Opt.* **11** 637–42
[16] Tien P K, Martin R J and Smolinsky G 1973 Formation of light-guiding interconnections in an integrated optical circuit by composite tapered-film coupling *Appl. Opt.* **12** 1909–16
[17] Sun M J and Muller M W 1977 Measurements on four-layer isotropic waveguides *Appl. Opt.* **16** 814–5
[18] Lockwood H F 1970 An efficient large optical cavity injection laser *Appl. Phys. Lett.* **17** 499–502
[19] Polky J N and Mitchell G L 1974 Metal-clad planar dielectric waveguide for integrated optics *J. Opt. Soc. Am.* **64** 274–9
[20] Scifres D R, Streifer W and Burnham R D 1976 Leaky wave room-temperature double heterostructure GaAs: GaAlAs diode laser *Appl. Phys. Lett.* **29** 23–5
[21] Southwell W H 1977 Index profiles for generalized Luneburg lenses and their use in planar optical waveguides *J. Opt. Soc. Am.* **67** 1010–4
[22] Reisinger A 1973 Characteristics of optical guided modes in lossy waveguides *Appl. Opt.* **12** 1015–25
[23] Rashleigh S C 1976 Four-layer metal-clad thin film optical waveguides *Opt. Quantum Electron.* **8** 49–60
[24] Cherny V V, Juravlev G A, Kirpa A I, Rylov I L and Tjoy V P 1979 Self-filtering multilayer S-waveguides with absorption and radiation losses *IEEE J. Quantum Electron.* **15** 1401–4
[25] Tabib-Azar M 1995 *Integrated Optics, Microstructures, and Sensors* (New York: Springer)
[26] Carson R F and Batchman T E 1990 Multimode phenomena in semiconductor-clad dielectric optical waveguide structures *Appl. Opt.* **29** 2769–80
[27] Stiens J, De Tandt C, Ranson W, Vounckx R, Demeester P and Moerman I 1994 Experimental study of an $In_{0.53}Ga_{0.47}As$-InP resonant plasma waveguide modulator for medium-infrared light *Appl. Phys. Lett.* **65** 2341–3
[28] Stiens J, Vounckx R, Veretennicoff I, Voronko A and Shkerdin G 1997 Slab plasmon polaritons and waveguide modes in four-layer resonant semiconductor waveguides *J. Appl. Phys.* **81** 1–10
[29] Zvezdin A K and Kotov V A 1997 *Modern Magnetooptics and Magnetooptical Materials* (Bristol: Institute of Physics)
[30] Priye V, Pal B P and Thyagarajan K 1998 Analysis and design of a novel leaky YIG film guided wave optical isolator *J. Lightwave Technol.* **16** 246–50
[31] Augućiuk E and Biniecki G 2009 Investigation of parameters of multimode four-layer waveguide structures and their influence on light propagation *Photonics Lett. Pol.* **1** 124–6
[32] Sylgacheva D A, Khokhlov N E, Kalish A N and Belotelov V I 2016 Magnetic control of waveguide modes of Bragg structures *J. Phys. Conf. Ser.* **714** 012016
[33] Khosravi S, Rostami A, Rostami G and Dolatyari M 2015 Nanocomposite multilayer structure for broadband MIR negative refractive index *J. Lightwave Technol.* **33** 4171–5

[34] Khokhlov N E *et al* 2015 Photonic crystals with plasmonic patterns: novel type of the heterostructures for enhanced magneto-optical activity *J. Phys. D: Appl. Phys.* **48** 95001
[35] Dotsch H, Bahlmann N, Zhuromskyy O, Hammer M, Wilkens L, Gerhardt R, Hertel P and Popkov A F 2005 Applications of magneto-optical waveguides in integrated optics: review *J. Opt. Soc. Am.* B **22** 240–53
[36] Rao R and Tang T 2012 Study of an active hybrid gap surface plasmon polariton waveguide with nanoscale confinement size and low compensation gain *J. Phys. D: Appl. Phys.* **45** 245101
[37] Alaeian H and Dionne J A 2014 Non-Hermitian nanophotonic and plasmonic waveguides *Phys. Rev.* B **89** 1–9
[38] Smirnova D A, Iorsh I V, Shadrivov I V and Kivshar Y S 2014 Multilayer graphene waveguides *JETP Lett.* **99** 456–60
[39] Chen L, Cao Z, Ou F, Li H, Shen Q and Qiao H 2007 Observation of large positive and negative lateral shifts of a reflected beam from symmetrical metal-cladding waveguides *Opt. Lett.* **32** 1432–4
[40] Chen L 2012 Optical devices based on symmetrical metal cladding waveguides *Optical Devices in Communication and Computation* ed P Xi (Rijeka: InTech) pp 127–52
[41] Rytov S M 1956 Electromagnetic properties of a finely stratified medium *Sov. Phys.—JETP* **2** 446–75
[42] Brekhovskikh L M 1980 *Waves in Layered Media* (New York: Academic)
[43] Lyubchanskii I L, Dadoenkova N N, Lyubchanskii M I, Shapovalov E A and Rasing T 2003 Magnetic photonic crystals *J. Phys. D: Appl. Phys.* **36** R277–87
[44] Randoshkin V V and Chervonenkis A Y 1990 *Applied Magneto-Optics* (Moscow: Energoatomizdat) (in Russian)
[45] Gurevich A G and Melkov G A 1996 *Magnetization Oscillations and Waves* (New York: CRC Press)
[46] Agranovich V M and Kravtsov V E 1985 Notes on crystal optics of superlattices *Solid State Commun.* **55** 85–90
[47] Yariv A and Yeh P 2007 *Photonics: Optical Electronics in Modern Communications* (New York: Oxford University)
[48] Goncharenko A M and Karpenko V A 1983 *Fundamentals of the Optical Waveguides Theory* (Minsk: Nauka i Tekhnika) (in Russian)
[49] Shutyi A M, Sannikov D G and Sementsov D I 1999 Waveguide modes of the light propagating in four-layer planar structures *J. Commun. Technol. Electron.* **44** 395–400
[50] Adams M J 1981 *An Introduction to Optical Waveguides* (New York: Wiley)
[51] Johnson B and Walton A K 1965 The infra-red refractive index of garnet ferrites *Br. J. Appl. Phys.* **16** 475–7
[52] Wood D L and Nassau K 1990 Optical properties of gadolinium gallium garnet *Appl. Opt.* **29** 3704–7
[53] Malitson I H 1965 Interspecimen comparison of the refractive index of fused silica *J. Opt. Soc. Am.* **55** 1205–9
[54] Devore J R 1951 Refractive indices of rutile and sphalerite *J. Opt. Soc. Am.* **41** 416–9
[55] Torfeh M and Le Gall H 1981 Theoretical analysis of hybrid modes of magnetooptical waveguides *Phys. Status Solidi* **63** 247–58
[56] Li B and Ju H 2013 Label-free optical biosensors based on a planar optical waveguide *Biochip J.* **7** 295–318
[57] Visnovsky S 2006 *Optics in Magnetic Multilayers and Nanostructures* (New York: Taylor and Francis)
[58] Jin C-Y and Wada O 2014 Photonic switching devices based on semiconductor nano-structures *J. Phys. D: Appl. Phys.* **47** 133001